

Numerical simulation of streamer evolution in surface dielectric barrier discharge with electrode-array

Cite as: J. Appl. Phys. **128**, 093301 (2020); <https://doi.org/10.1063/5.0013594>

Submitted: 15 May 2020 • Accepted: 07 August 2020 • Published Online: 01 September 2020

 Jiao Zhang,  Yanhui Wang,  Dezhen Wang, et al.



View Online



Export Citation



CrossMark

ARTICLES YOU MAY BE INTERESTED IN

[Plasma characteristics and mode transition of atmospheric pressure gas-liquid discharge oxygen plasma](#)

Journal of Applied Physics **128**, 093303 (2020); <https://doi.org/10.1063/5.0008941>

[Ionization wave propagation in a He plasma jet in a controlled gas environment](#)

Journal of Applied Physics **128**, 083301 (2020); <https://doi.org/10.1063/5.0020264>

[Microwave absorption and optical emission spectrometry analyses of ambient air plasmas induced by pulsed electron beams](#)

Journal of Applied Physics **128**, 093304 (2020); <https://doi.org/10.1063/5.0015482>



Applied Physics
Reviews

Read. Cite. Publish. Repeat.

19.162

2020 IMPACT FACTOR*



Numerical simulation of streamer evolution in surface dielectric barrier discharge with electrode-array

Cite as: J. Appl. Phys. 128, 093301 (2020); doi: 10.1063/5.0013594

Submitted: 15 May 2020 · Accepted: 7 August 2020 ·

Published Online: 1 September 2020



Jiao Zhang,¹ Yanhui Wang,¹ Dezhen Wang,¹ and Demetre J. Economou^{2,a)}

AFFILIATIONS

¹School of Physics, Dalian University of Technology, Dalian 116024, People's Republic of China

²Department of Chemical and Biomolecular Engineering, Plasma Processing Laboratory, University of Houston, Houston, Texas 77204, USA

^{a)}Author to whom correspondence should be addressed: economou@uh.edu

ABSTRACT

Atmospheric pressure surface dielectric barrier discharges (SDBDs) may be composed of streamers fast propagating along a dielectric surface in ambient air, producing reactive oxygen and nitrogen species, and inducing a force on the neutral gas, which can find applications, respectively, in plasma medicine and aerodynamics. In this work, a two-dimensional self-consistent fluid model was developed to study SDBDs with an electrode-array. Emphasis was placed on the interaction of counter-propagating streamers and discharge uniformity for different applied voltages and geometric configurations of the electrode-array. When two counter-propagating streamers collide, the streamers come to a stop within a certain (ultimate) distance between the streamer heads. Optimizing the applied voltages is a convenient way to improve uniformity, making the streamer heads reach a minimum distance between each other. Shortening the electrode spacing can simultaneously shorten the streamer length and the ultimate distance between streamers. Under certain discharge parameters (such as applied voltage), there exists an optimum electrode spacing maximizing uniformity.

Published under license by AIP Publishing. <https://doi.org/10.1063/5.0013594>

I. INTRODUCTION

Interest continues to increase in low-temperature, non-equilibrium, atmospheric-pressure plasmas due to a wide range of current and potential applications, including materials processing, environmental remediation, plasma medicine,^{1–3} and aerodynamic flow control.^{4,5} Direct discharges in ambient air provide a convenient and cost-effective way to generate plasmas in order to realize these and other applications. A variety of configurations, such as pin-electrode discharges, atmospheric pressure plasma jets (APPJs), and dielectric barrier discharges (DBDs), have received much attention.^{6–8} Volume DBDs most often consist of two parallel plate electrodes, with at least one of them covered by a dielectric layer. DBDs have the advantage of generating a stable and uniform plasma, helping to avoid transition to a high temperature arc with a constricted channel. Surface dielectric barrier discharges (SDBDs), also known as surface micro-discharges, are geometrically asymmetric DBDs with one electrode embedded in a dielectric and the

other electrode (or electrode-array) placed on the dielectric surface and exposed to ambient air. SDBDs have the advantages of high energy efficiency and direct discharge in ambient air with no need for pumps or noble gases.⁸

In a SDBD, the discharge propagates on the dielectric exposed to the ambient gas. For a SDBD with positive polarity, a positive (cathode) streamer propagates along the dielectric surface, charging the dielectric as the streamer passes by. In the streamer body, electrons, cations, anions, and reactive oxygen and nitrogen species (RONS) are produced. Ions are important for producing ionic wind with application in actuators for flow control, e.g., controlling laminar to turbulent flow transition,^{9–11} while RONS are crucial to plasma medicine.¹² Positive and negative polarity SDBDs are compared in Refs. 13–15. A streamer-like discharge is produced by a positive voltage pulse applied to the exposed electrode(s), while a diffuse discharge is produced by a negative voltage.^{16,17}

In order to increase the area affected by the discharge, electrode-arrays have been implemented.^{18–21} In these cases, the

discharge uniformity and the interaction among streamers are of primary importance. The interaction of co-propagating or counter-propagating streamers and the discharge uniformity have been studied experimentally and computationally in systems such as APPJs^{22–25} and multi-pin electrode discharges.^{26,27} However, the issues of streamer interaction and discharge uniformity have not received much attention in SDBDs with electrode-arrays.

In this work, a two-dimensional self-consistent fluid model was developed to study SDBDs with electrode-arrays. A single electrode was considered first as a base case for comparison. The spatiotemporal distributions of electron density and electric field were studied as streamers propagated along the dielectric surface. For SDBD with electrode-array, the effect of voltage and electrode geometric configuration on counter-propagating streamers and discharge uniformity, of importance for large area processing, was investigated.

II. COMPUTATIONAL MODEL

A. Mathematical model equations

Figure 1 shows a side view of the SDBD considered in this work, depicting the case of a single exposed electrode. The simulation domain was 10 mm (length) × 3 mm (height) in Cartesian x - y coordinates. A two-dimensional (2D) system was assumed. For this approximation to be correct, the dimension perpendicular to the plane of the paper (the z -direction) must be long enough for edge effects to be negligible. Also, if filaments do not travel in the z -direction the discharge can be thought of as continuous in the x - y plane by averaging over the randomly generated filaments. Thus, a 2D representation may be applicable. For example, a 3D simulation of a SDBD was reported by Nishida *et al.*²⁸ The authors concluded that the body force calculated by the 3D simulation, when averaged over the spanwise direction, produced results consistent with the results of a 2D simulation of their SDBD system.

The grounded electrode was underneath the dielectric, all along its length. The exposed electrode was placed on the upper left surface of the dielectric. The 2D fluid model included continuity equations for both charged and neutral species, Eq. (1), the drift-diffusion approximation for charged species, Eqs. (2) and (3), and diffusion flux for neutral species, Eq. (4),

$$\frac{\partial n_j}{\partial t} + \nabla \cdot \mathbf{j}_j = S_j, \quad (1)$$

$$\mathbf{j}_{e,-} = -\mu_{e,-} \mathbf{E} n_{e,-} - D_{e,-} \nabla n_{e,-}, \quad (2)$$

$$\mathbf{j}_+ = \mu_+ \mathbf{E} n_+ - D_+ \nabla n_+, \quad (3)$$

$$\mathbf{j}_m = -D_m \nabla n_m, \quad (4)$$

where subscripts e , $-$, $+$, and m represent electrons, negative ions, positive ions, and neutral species, respectively. n is the number density (cm^{-3}) and \mathbf{j} is the flux ($\text{cm}^{-2} \text{s}^{-1}$). \mathbf{E} is the electric field vector, μ is mobility, D is the diffusion coefficient, and S_j ($j = e, +, -, m$) is the net source of species j , derived from the chemical reactions that produce and consume that species. For S_e and $S_{\text{O}_2^+}$, the contribution of photoionization was included by

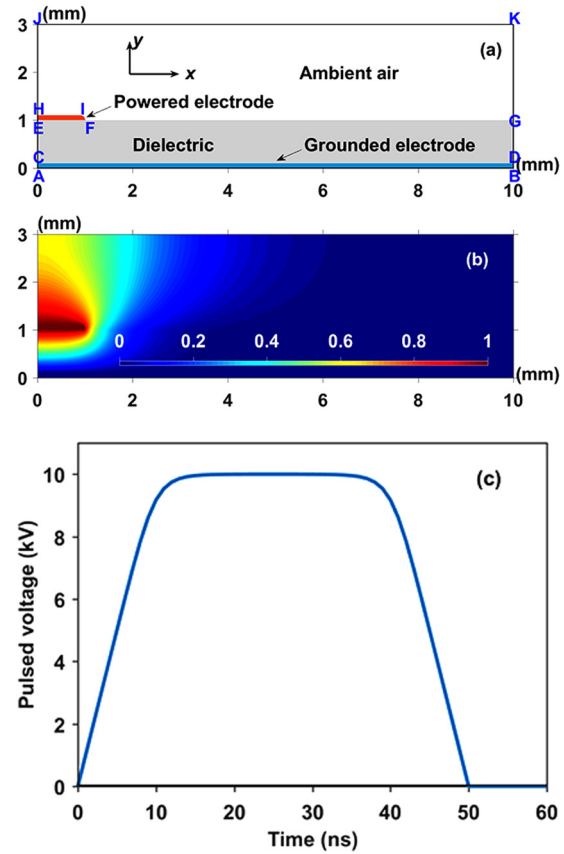


FIG. 1. (a) Schematic of the geometry of the surface dielectric barrier discharge with a single powered (exposed) electrode. (b) Laplacian potential distribution due to the electrode configuration only (zero space charge everywhere). A constant potential of +1 was applied to the powered electrode. (c) Voltage pulse applied to the powered electrode during SDBD operation. The simulation was continued for 10 ns after the voltage had returned to zero (a total of 60 ns for a complete extended pulse).

the three-exponential Helmholtz method.²⁹ Photoionization increases the source of electrons and ions, but it is not essential for streamer propagation as long as the electron density exceeds a minimum value.³⁰ Boundary conditions are summarized in Table I.

The electric potential (φ) was found by solving Poisson's equation,^{15,31,32}

$$\nabla \cdot (\epsilon_r \nabla \varphi) = -\frac{\rho_v + \delta_s \sigma_s}{\epsilon_0}. \quad (5)$$

Here, ρ_v is the net space (volumetric) charge density, and σ_s is the surface charge density on the exposed dielectric, ignoring any polarization charges in the bulk dielectric. δ_s is the Dirac delta function, ϵ_0 is the vacuum permittivity, and ϵ_r is the relative permittivity, which is 1.0 for air and 7.5 for the dielectric used in the present work. Boundary conditions for Eq. (5) are also shown in Table I.

TABLE I. Boundary conditions on electric potential (φ) and species densities (n). V_a is the potential applied to the powered electrode, see Fig. 1(c). The segments of the system geometry shown in the top row of this table are identified by referring to Fig. 1(a). For example, CD identifies the top surface of the grounded electrode.

	CD	HIFE	FG	JH (EC)	JK	KG (GD)
φ	0	V_a	...	$\frac{\partial \varphi}{\partial x} = 0$	$\frac{\partial \varphi}{\partial y} = 0$	$\frac{\partial \varphi}{\partial x} = 0$
n	0	0	Eq. (7) for n_e .	$\frac{\partial n}{\partial x} = 0$	$\frac{\partial n}{\partial y} = 0$	$\frac{\partial n}{\partial x} = 0$

The dielectric surface charge was calculated by

$$\frac{\partial \sigma_s}{\partial t} = -e \left[\left(\sum j_+ - \sum j_- - j_e \right) \cdot \mathbf{n} \right], \quad (6)$$

where the summations are over all positive and negative ions. Secondary electron emission due to positive ion bombardment on the dielectric surface was considered, yielding an electron flux perpendicular to the surface,

$$\mathbf{j}_e \cdot \mathbf{n} = \left(-\mu_e E n_e - \alpha_s \gamma \sum j_+ \right) \cdot \mathbf{n}, \quad (7)$$

where \mathbf{n} is the unit vector perpendicular to the surface, pointing toward the surface, γ is the secondary electron emission coefficient (assumed to be 0.01), and α_s is a switching factor (either 0 or 1) depending on the dot product $\mathbf{E} \cdot \mathbf{n}$, and defined as unity when the positive ion flux due to drift is directed toward the surface.

Both the initial densities of electrons and sum of positive ions were taken to be uniform at $1 \times 10^7 \text{ cm}^{-3}$. This initial charge density may be due to background ionization or as residual charge left by the previous potential pulse. The initial density of N_2^+ was taken to be four times the initial density of O_2^+ to reflect the air composition.

B. Method of solution

The above set of Eqs.(1)–(4) was solved by a finite difference method, using a Scharfetter–Gummel scheme³³ with an alternating direction implicit (ADI) technique. An electron energy equation was not solved. Instead, the “local field” approximation was invoked, whereby the rate coefficients of electron impact reactions, and electron transport properties (mobility, diffusivity), at a given spatial point and time are a function of the reduced electric field (E/N) at that point and time. This is a reasonable approximation due to the high collisionality at atmospheric pressure, and it is used widely in the literature.³⁴

The working gas was artificial air (80% N_2 + 20% O_2). The chemistry model (Table II) included 78 reactions and 17 species: electrons, N_2 , $\text{N}_2(A^3\Sigma_u^+)$, $\text{N}_2(a^1\Sigma_u^-)$, N_2^+ , N_4^+ , N , O_2 , $\text{O}_2(a^1\Delta_g)$, $\text{O}_2(b^1\Sigma_u^+)$, O_2^+ , O_4^+ , O^- , O_2^- , O , O_3 , and NO . The rate coefficients of electron impact reactions were obtained by solving Boltzmann’s equation using BOLSIG+.³⁵ Cross sections for elastic collisions, rotational, vibrational and electronic excitations, dissociations, and ionizations were taken from the Morgan, TRINITI, and Phelps databases.^{36–38} Solution of Boltzmann’s equation, for different values of the reduced electric field (E/N), provided the electron

energy distribution function (EEDF), and therefrom the electron mean energy, electron transport coefficients, and electron impact reaction rate coefficients as a function of E/N . Transport coefficients for ions and neutrals were estimated following Ref. 39.

For grid points adjacent to the electrode, the Ghost Fluid Method (GFM)⁴⁰ was used in the finite difference scheme. The potential of the grounded (embedded) electrode was set to zero, while the exposed electrode was powered by a positive voltage pulse with 10 ns rise time, 10 ns fall time, and 30 ns plateau [Fig. 1(c)]. The simulation was continued for 10 more ns after the voltage had returned to zero. Poisson’s equation was solved using a SuperLU solver,⁴¹ which is computationally more efficient than standard iterative methods. The rectangular finite difference grid was uniform in the x -direction, but non-uniform in the y -direction. A denser grid (cell size $2.5 \times 5 \mu\text{m}^2$ in x and y directions, respectively) was used in the space where the streamer was expected to propagate. For the base case conditions, discretization led to a total of $\sim 900\,000$ degrees of freedom.

The base case parameter values were as follows: gas pressure 760 Torr, gas temperature 300 K, plateau of applied voltage pulse 10 kV, electrode width 1 mm, and spacing between the electrode edges of the two electrode-array (see below) 8 mm.

When the potential of the powered (exposed) electrode was set to a constant value of +1, and the space charge was set to zero everywhere, the spatial distribution of the (under these conditions) Laplacian potential, governed by the electrode structure alone (no plasma), is shown in Fig. 1(b).

III. RESULTS AND DISCUSSION

A. Single exposed electrode

The following spatiotemporal profiles show simulation results in the region of 10 mm (width) \times 1 mm (height) of the computational domain, i.e., only the lower half of the gas phase in Fig. 1(a) is shown. The streamer fits comfortably within this region. The spatiotemporal evolution of electron density and the magnitude of the reduced electric field E/N , where N is the neutral gas density (at 760 Torr and 300 K), are shown in Fig. 2. A streamer starts at the right edge of the exposed electrode, following gas breakdown, within the first 10 ns of the applied voltage pulse, and propagates along the dielectric surface. Streamer propagation is driven by a high electric field (max E/N is 1411 Td, 1 Td = 10^{-17} V cm^2). The electric field grows high in the space between the streamer and the dielectric wall due to the formation of a sheath. The electric field in the streamer body is relatively low (~ 20 Td), below the dielectric strength of air. The peak electron density at 10 ns and 45 ns into the pulse is $1 \times 10^{14} \text{ cm}^{-3}$ and $5 \times 10^{13} \text{ cm}^{-3}$, respectively. At 45 ns (ramp down of applied voltage pulse), the streamer length is ~ 5.5 mm. During the falloff of the applied voltage, the applied electric field keeps decreasing, while the electric field due to the combination of positive space charge, and positive charge accumulated on the dielectric surface keeps increasing, to the point that the potential of the dielectric surface exceeds that of the exposed electrode, and the electric field reverses direction (“second stroke,” see below). This occurs at around 45 ns into the pulse. This reversal is accompanied by a strengthening electric field that initially appears near the exposed electrode. The electric field then increases further

TABLE II. Artificial air (80% N₂ + 20% O₂) plasma chemistry.

Index	Reaction	Rate coefficient ^a	Threshold ^a	Reference
<i>Nitrogen chemistry</i>				
R1	$e + N_2 \rightarrow e + N_2$	Bolsig+&Morgan database	...	35,36
R2	$e + N_2 \rightarrow e + N_2(\text{rot})$	Bolsig+&Morgan database	0.02	35,36
R3	$e + N_2 \rightarrow e + N_2(v1)$	Bolsig+&Morgan database	0.29	35,36
R4	$e + N_2 \rightarrow e + N_2(v1)$	Bolsig+&Morgan database	0.291	35,36
R5	$e + N_2 \rightarrow e + N_2(v2)$	Bolsig+&Morgan database	0.59	35,36
R6	$e + N_2 \rightarrow e + N_2(v3)$	Bolsig+&Morgan database	0.88	35,36
R7	$e + N_2 \rightarrow e + N_2(v4)$	Bolsig+&Morgan database	1.17	35,36
R8	$e + N_2 \rightarrow e + N_2(v5)$	Bolsig+&Morgan database	1.47	35,36
R9	$e + N_2 \rightarrow e + N_2(v6)$	Bolsig+&Morgan database	1.76	35,36
R10	$e + N_2 \rightarrow e + N_2(v7)$	Bolsig+&Morgan database	2.06	35,36
R11	$e + N_2 \rightarrow e + N_2(v8)$	Bolsig+&Morgan database	2.35	35,36
R12	$e + N_2 \rightarrow e + N_2(A^3\Sigma_u^+ \ v = 0 - 4)$	Bolsig+&Morgan database ^b	6.17	35,36
R13	$e + N_2 \rightarrow e + N_2(A^3\Sigma_u^+ \ v = 5 - 9)$	Bolsig+&Morgan database ^b	7	35,36
R14	$e + N_2 \rightarrow e + N_2(B^3\Pi_g)$	Bolsig+&Morgan database	7.35	35,36
R15	$e + N_2 \rightarrow e + N_2(W^3\Delta_g^-)$	Bolsig+&Morgan database	7.36	35,36
R16	$e + N_2 \rightarrow e + N_2(A^3\Sigma_u^+ \ v = 10-)$	Bolsig+&Morgan database ^b	7.8	35,36
R17	$e + N_2 \rightarrow e + N_2(B^3\Sigma)$	Bolsig+&Morgan database	8.16	35,36
R18	$e + N_2 \rightarrow e + N_2(a^1\Sigma_u^-)$	Bolsig+&Morgan database	8.4	35,36
R19	$e + N_2 \rightarrow e + N_2(a^1\Pi)$	Bolsig+&Morgan database	8.55	35,36
R20	$e + N_2 \rightarrow e + N_2(w^1\Delta)$	Bolsig+&Morgan database	8.89	35,36
R21	$e + N_2 \rightarrow e + N_2(C^3\Pi)$	Bolsig+&Morgan database	11.03	35,36
R22	$e + N_2 \rightarrow e + N_2(E^3\Sigma)$	Bolsig+&Morgan database	11.88	35,36
R23	$e + N_2 \rightarrow e + N_2(a^1\Sigma)$	Bolsig+&Morgan database	12.25	35,36
R24	$e + N_2 \rightarrow 2e + N_2^+$	Bolsig+&Morgan database	15.6	35,36
R25	$e + N_2 \rightarrow e + 2N$	$6.3 \times 10^{-12} T_e^{-1.6} \exp(-9.8/T_e)$	9.8	42
R26	$e + N_2 \rightarrow e + N + N(13 \text{ eV})$	Bolsig+&Morgan database	13.0	35,36
R27	$N_2(A^3\Sigma_u^+) + N_2(a^1\Sigma_u^-) \rightarrow N_4^+ + e$	5×10^{-11}	...	43
R28	$2N_2(a^1\Sigma_u^-) \rightarrow N_4^+ + e$	2×10^{-10}	...	43
R29	$N_2^+ + N_2 + M \rightarrow N_4^+ + M$	6.4×10^{-30}	...	42
R30	$N_4^+ + e \rightarrow 2N_2$	$2 \times 10^{-6} (0.026/T_e)^{0.5}$...	43
R31	$e + N_2^+ \rightarrow 2N$	$2.8 \times 10^{-7} (0.026/T_e)^{0.5}$...	44
R32	$e + N_2^+ + M \rightarrow N_2 + M$	$6 \times 10^{-27} (0.026/T_e)^{1.5}$...	43
<i>Oxygen chemistry</i>				
R33	$e + O_2 \rightarrow e + 2O$	Bolsig+&TRINITY Database ^b	5.58	35,37
R34	$e + O_2 \rightarrow e + O + O(1D)$	Bolsig+&TRINITY Database ^b	8.4	35,37
R35	$e + O_2 \rightarrow e + O_2$	Bolsig+&Phelps Database	...	35,38
R36	$e + O_2 \rightarrow e + O_2(\text{rot})$	Bolsig+&Phelps Database	0.02	35,38
R37	$e + O_2 \rightarrow e + O_2(v1)$	Bolsig+&Phelps Database	0.19	35,38
R38	$e + O_2 \rightarrow e + O_2(v1)$	Bolsig+&Phelps Database	0.19	35,38
R39	$e + O_2 \rightarrow e + O_2(v2)$	Bolsig+&Phelps Database	0.38	35,38
R40	$e + O_2 \rightarrow e + O_2(v2)$	Bolsig+&Phelps Database	0.38	35,38
R41	$e + O_2 \rightarrow e + O_2(v3)$	Bolsig+&Phelps Database	0.57	35,38
R42	$e + O_2 \rightarrow e + O_2(v4)$	Bolsig+&Phelps Database	0.75	35,38
R43	$e + O_2 \rightarrow e + O_2(a^1\Delta_g)$	Bolsig+&Phelps Database ^b	0.98	35,38
R44	$e + O_2 \rightarrow e + O_2(b^1\Sigma_u^+)$	Bolsig+&Phelps Database ^b	1.63	35,38
R45	$e + O_2 \rightarrow e + O_2(\text{exc})$	Bolsig+&Phelps Database	4.5	35,38
R46	$e + O_2 \rightarrow e + O_2(\text{exc})$	Bolsig+&Phelps Database	6	35,38
R47	$e + O_2 \rightarrow e + O_2(\text{exc})$	Bolsig+&Phelps Database	8.4	35,38
R48	$e + O_2 \rightarrow e + O_2(\text{exc})$	Bolsig+&Phelps Database	9.97	35,38
R49	$e + O_2 \rightarrow 2e + O_2^+$	Bolsig+&Phelps Database ^b	12.06	35,38
R50	$e + O_2 \rightarrow O^- + O$	Bolsig+&Phelps Database ^b	3.6	35,38
R51	$e + O_2 + M \rightarrow O_2^- + M$	Bolsig+&Phelps Database ^b	-0.43	35,38

TABLE II. (Continued.)

Index	Reaction	Rate coefficient ^a	Threshold ^a	Reference
R52	$O_2^+ + O_2 + M \rightarrow O_4^+ + M$	2.4×10^{-30}	...	45
R53	$O_4^+ + O \rightarrow O_2^+ + O_3$	3×10^{-10}	...	46
R54	$O^- + O_2 \rightarrow e + O_3$	$5 \times 10^{-15} (T_g/300)^{0.5}$...	47
R55	$O_2^- + O \rightarrow e + O_3$	$1.5 \times 10^{-10} (T_g/300)^{0.5}$...	47
R56	$e + O_2^+ \rightarrow 2O$	$1.2 \times 10^{-8} T_e^{-0.7}$...	47
R57	$e + O_4^+ \rightarrow 2O_2$	$1.4 \times 10^{-6} (0.026/T_e)^{0.5}$...	45
R58	$O^- + O_2^+ \rightarrow O + O_2$	$2 \times 10^{-7} (T_g/300)^{-1}$...	47
R59	$O^- + O_2^+ \rightarrow 3O$	1×10^{-7}	...	47
R60	$O^- + O_4^+ \rightarrow O_3 + O_2$	4×10^{-7}	...	46
R61	$O_2^- + O_4^+ \rightarrow 3O_2$	1×10^{-7}	...	45
R62	$O_2^- + O_4^+ + M \rightarrow 3O_2 + M$	2×10^{-25}	...	45
R63	$O_2^- + O_2^+ \rightarrow 2O_2$	2×10^{-7}	...	48
R64	$O_2^- + O_2^+ \rightarrow O_2 + 2O$	1×10^{-7}	...	47
R65	$O_2^- + O_2^+ + M \rightarrow 2O_2 + M$	2×10^{-25}	...	45,48
R66	$O + O_2 + N_2 \rightarrow O_3 + N_2$	$1.1 \times 10^{-34} \exp(510/T_g)$...	46
R67	$O + 2O_2 \rightarrow O_3 + O_2$	$6 \times 10^{-34} (T_g/300)^{-2.8}$...	47
R68	$O_2 + 2O \rightarrow O_3 + O$	$3.4 \times 10^{-34} (T_g/300)^{-1.2}$...	47
R69	$O + O_2 + O_3 \rightarrow 2O_3$	$2.3 \times 10^{-35} \exp(-1057/T_g)$...	46
R70	$O + O_3 \rightarrow 2O_2$	$8 \times 10^{-12} \exp(-2060/T_g)$...	47,49
<i>Nitrogen–oxygen interactions</i>				
R71	$N + O + M \rightarrow NO + M$	$5.5 \times 10^{-33} \exp(155/T_g)$...	50
R72	$N_2^+ + O^- \rightarrow N_2 + O$	$2 \times 10^{-7} (T_g/300)^{-0.5}$...	43
R73	$N_2^+ + O_2^- \rightarrow N_2 + O_2$	$2 \times 10^{-7} (T_g/300)^{-0.5}$...	43
R74	$N_4^+ + O^- \rightarrow 2N_2 + O$	1×10^{-7}	...	43
R75	$N_4^+ + O_2^- \rightarrow 2N_2 + O_2$	1×10^{-7}	...	43
R76	$O^- + N_2(A^3\Sigma_u^+) \rightarrow N_2 + O + e$	2.2×10^{-9}	...	51
R77	$O_2^- + N_2(A^3\Sigma_u^+) \rightarrow N_2 + O_2 + e$	2.1×10^{-9}	...	51
R78	$N_2(A^3\Sigma_u^+) + O_2 \rightarrow N_2 + 2O$	$5 \times 10^{-12} \exp(-210/T_g)$...	51

^aRate coefficients are in $\text{cm}^3 \text{s}^{-1}$ for two-body reactions, and $\text{cm}^6 \text{s}^{-1}$ for three-body reactions. T_e is in eV; T_g is 300 K. Threshold energy is in eV.

^bThe electron impact reaction rate coefficients were tabulated as a function of reduced electric field (E/N) and interpolated for use in the fluid model.

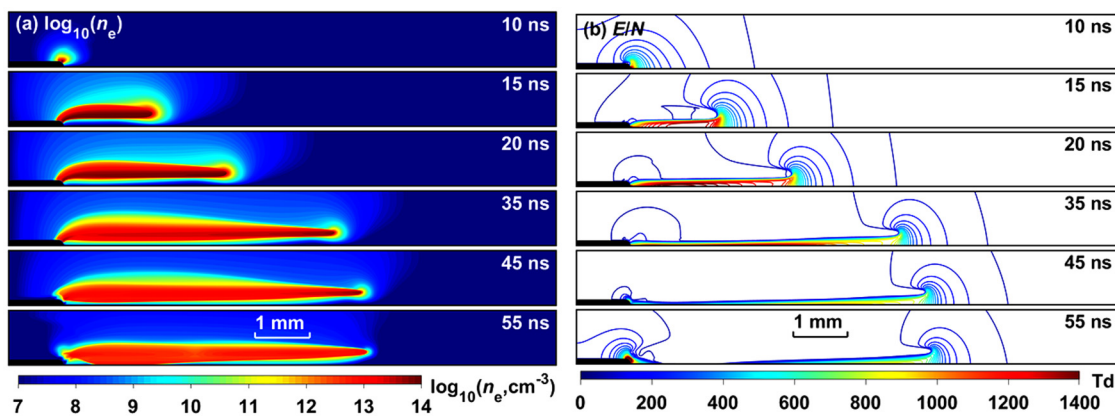


FIG. 2. Spatial distribution of $\log_{10}(n_e)$ with n_e in cm^{-3} (a) and magnitude of the reduced electric field E/N (b), at different times during a voltage pulse. The maximum E/N is 1411 Td. The spacing between adjacent contours is 50 Td. Parameters were at their base case values. The 1 mm scale is shown at the bottom of the figure. Color scales of the E/N strength and the \log_{10} of the electron density are also shown.

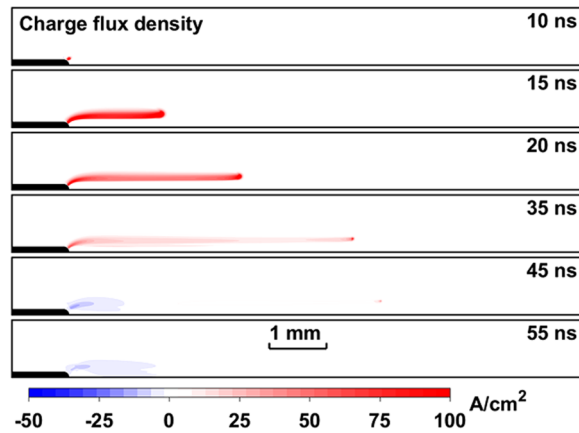


FIG. 3. Spatial distribution of the x -component of the charge flux for different times during a voltage pulse. Parameters were at their base case values. The 1 mm scale is shown at the bottom of the figure. A color scale of the charge flux is also shown.

(compare E/N at times of 45 and 55 ns in Fig. 2), before the electric field is eventually extinguished, shortly after the applied voltage has returned to zero.

Figure 3 shows the x -component of the charge flux $I_x = e(\sum j_{+x} - \sum j_{-x} - j_{ex})$ where the summations include negative ions (O_2^- and O^-) and positive ions (N_2^+ , O_2^+ , N_4^+ , and O_4^+). In Fig. 3, red and blue colors represent fluxes in the positive ($+x$) and negative ($-x$) directions, respectively. The fluxes of positive and negative charges are in opposite directions. In fact, the direction of flux depends on the direction of the electric field since drift dominates diffusion over the short (10 s of ns) time scales examined. At 45 ns (the falling edge of the voltage pulse), the fluxes reverse the direction following the reversal of the electric field. This reversal has been referred to as the “second stroke,”^{13,52} and the main streamer propagation has been referred to as the “first stroke.” The second stroke is accompanied by a reversal of the current in the voltage-current ($V-I$) characteristic, caused by a reversal of the electric field, due to progressively higher influence by the space charge and accumulated surface charge, as the applied voltage keeps falling. In the second stroke, there is no streamer

propagation. The second stroke behaves like a “diffuse” discharge as would be generated by a negative voltage pulse applied to the exposed electrode.

The charge density along the dielectric surface at different times during an applied voltage pulse is shown in Fig. 4(a). The predicted charge density profiles are similar to those in Ref. 13. In a SDBD, driven by a positive voltage, the dielectric wall acquires a positive surface charge. This is because a streamer head with a positive space charge forms near the edge of the exposed electrode (the anode in this configuration). The space charge has to be large enough to create a strong electric field, causing ionization of the gas, so that the streamer can propagate. As the streamer slides along the dielectric, positive ions charge the surface of the dielectric positively. It should be noted that a sheath with a high electric field forms over the dielectric surface. The field is pointing toward the surface and opposes the motion of electrons and negative ions toward the dielectric, while facilitating the motion of positive ions toward the surface. The surface charge density keeps increasing even when the applied voltage is falling. The spatial extent of surface charges corresponds to the length of the streamer. Figure 4(b) shows the streamer propagation speed vs time, during a voltage pulse. The blue asterisks represent the streamer speed calculated by using the location of maximum x -directed component of the electric field (E_x) as the position of the streamer head. Gas breakdown occurs during the voltage ramp-up, and a streamer forms within ~ 10 ns. The streamer accelerates rapidly and reaches its maximum speed of 3.8×10^5 m/s, shortly after the voltage pulse has plateaued. Beyond that time, the streamer decelerates reaching a residual speed close to zero, ~ 10 ns after the end of the voltage pulse. These findings are in accord with simulation results¹⁵ as well as experimental observations.⁵²

Volumetric forces are crucial in applications of SDBDs as actuators for aerodynamic flow control. The volumetric force (N/cm^3) on the neutral gas is approximately $f = e(j_+/\mu_+ + j_e/\mu_e + j_-/\mu_-)$ ¹⁰ and is shown in Fig. 5. This force is attributed to momentum exchange between charged particles (positive ions, negative ions, and electrons) and the neutral gas. In the streamer body, the force due to positive ions is almost balanced by the force due to negative ions and electrons. At the streamer top, the force is such that it drags neutral gas away from the dielectric. This is a relatively weak force, however, and appears only at the beginning of the discharge, so it can be ignored. The main forces

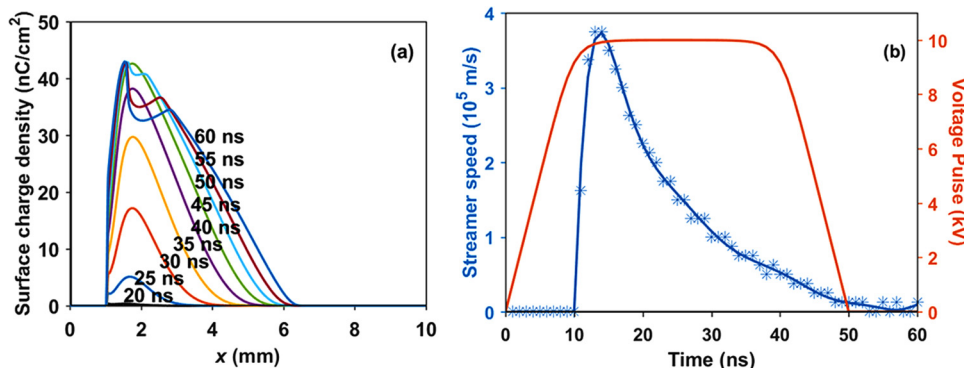


FIG. 4. (a) Surface charge density distribution along the dielectric at different times during a voltage pulse. The exposed electrode occupies the region $x = 0$ to $x = 1$ mm. (b) Streamer propagation speed as a function of time during a voltage pulse. The calculated speeds are shown as stars. The line is to guide the eye. The applied voltage pulse is also shown.

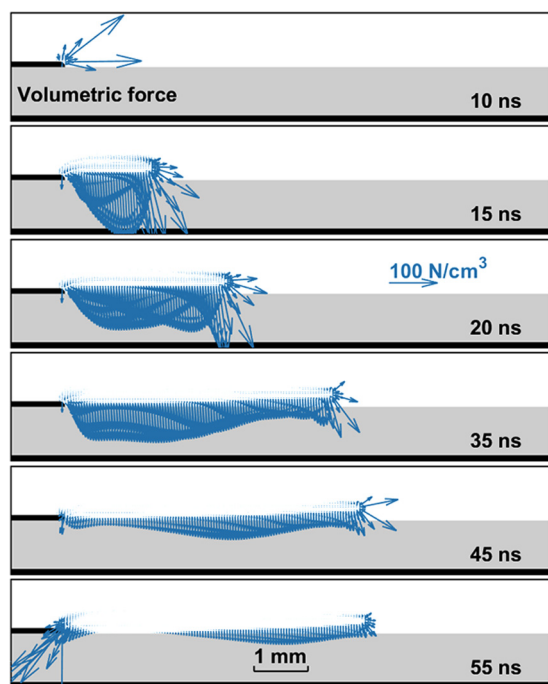


FIG. 5. Spatial distribution of the volumetric force on the neutral gas at different times during a voltage pulse. The force is proportional to the arrow length. The 100 N/cm^3 scale is also shown. Parameters were at their base case values. The 1 mm scale is shown at the bottom of the figure.

appear in the sheath separating the streamer from the dielectric floor and in the streamer head. The simulation results are similar to Ref. 9. The force in the sheath is perpendicular to the surface and pushes the neutral gas toward the dielectric. The magnitude and direction of this force remain almost constant as the active area increases by streamer propagation. The magnitude of the force at the streamer head has a significant forward component. Even at the falling edge of the voltage pulse, the force in the streamer head is still directed mainly downstream.⁹ Also apparent in Fig. 5 is the force at 55 ns (voltage at zero) with a large component in the minus- x direction due to field reversal (second stroke, see above). The forces created by the surface micro-discharge are of utmost importance in actuator control.

Figure 6 shows the spatiotemporal evolution of the N_2^+ , N_4^+ , and O_2^- ion densities. N_2^+ ions are produced by direct electron-impact ionization of N_2 (reaction R24 in Table II) in regions of high electric field (due to the relatively high ionization threshold). Therefore, the N_2^+ ion density exhibits a maximum at that location. N_2^+ ions are consumed by recombination and especially association reactions (R29) that produce N_4^+ . This is also an important positive ion with considerable number density that can exceed the density of N_2^+ . Since N_4^+ is not produced by electron impact ionization, its density does not show maxima at the streamer head. In fact, the density of this ion is much more uniform compared to N_2^+ . In addition to the association reaction,

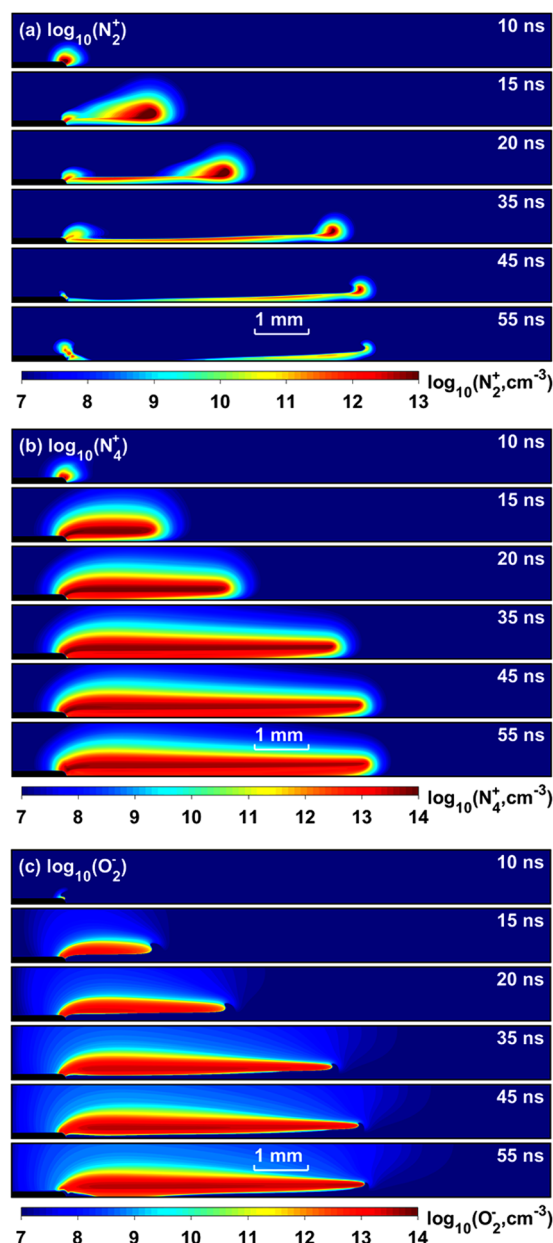


FIG. 6. Spatial distribution of the number density (\log_{10} scale) of N_2^+ (a), N_4^+ (b), and O_2^- (c), at different times during a voltage pulse. The particle density is in cm^{-3} . Parameters were at their base case values. The 1 mm scale is shown at the bottom of the figure. In each of the three figures, a color scale of the \log_{10} of the corresponding ion density is also shown.

N_4^+ is also produced by Penning ionization between the excited states of N_2 (R27 and R28). The rate of these reactions depends on the densities of $\text{N}_2(\text{A})$ and $\text{N}_2(\text{a})$ rather than the electric field. Being an electronegative gas, O_2 consumes electrons by attachment

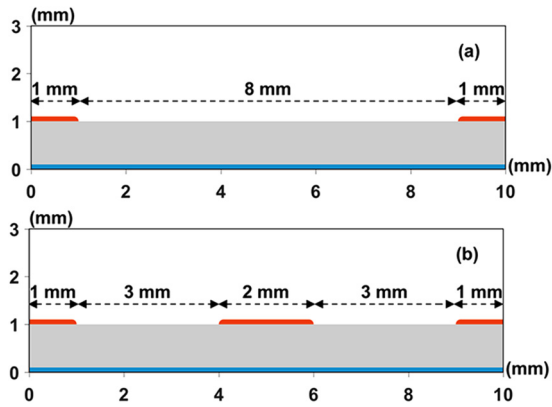


FIG. 7. Schematic of the geometry of the electrode-array of the surface dielectric barrier discharge with two (a), and three (b), exposed electrodes.

reactions to produce O_2^- and O^- . The spatial distribution of O_2^- is fairly uniform (Fig. 6, bottom), and its density is $\sim 10^{13} - 10^{14} \text{ cm}^{-3}$, comparable to the electron density.

B. Multiple exposed electrodes (electrode-arrays)

For treating relatively large areas, electrode-array, mesh electrode, and hollow electrode-array have been proposed.⁵³⁻⁵⁵ The simplest configuration of an electrode-array consists of a second exposed electrode placed on the dielectric above the right side of the grounded electrode, as shown in Fig. 7(a). When both electrodes are powered with the same positive voltage, two streamers will propagate symmetrically in opposite directions, facing each other. Provided the streamer heads are far apart, each streamer propagates independently of the other, and the results obtained for a single exposed electrode discussed above apply. To investigate the two electrode-array configuration, the electrodes were powered with an identical voltage pulse [shown in Fig. 1(c)] with a plateau

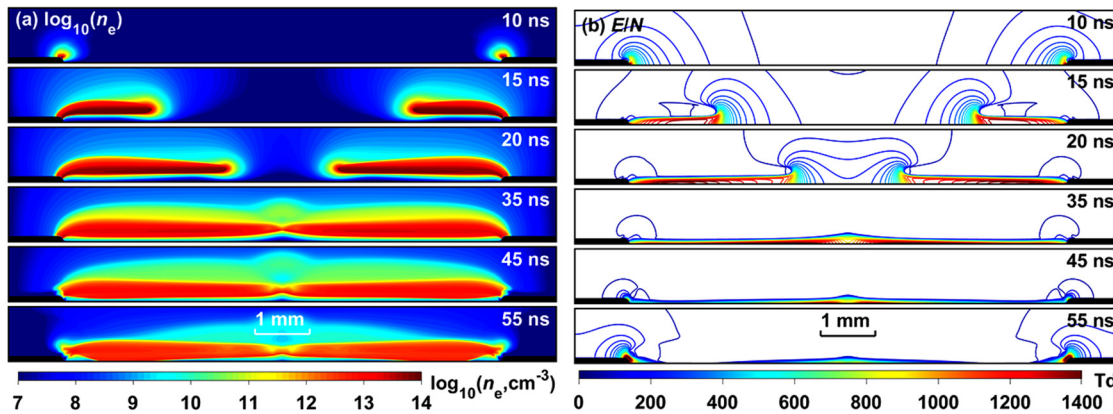


FIG. 8. Spatial distribution of $\log_{10}(n_e)$, n_e in cm^{-3} (a), and magnitude of reduced electric field E/N (b), for two exposed electrodes powered by identical voltage pulses (plateau voltage 10 kV). In (b), the spacing between adjacent contours is 50 Td. The 1 mm scale is shown at the bottom of the figure. Color scales of the E/N strength and the \log_{10} of the electron density are also shown.

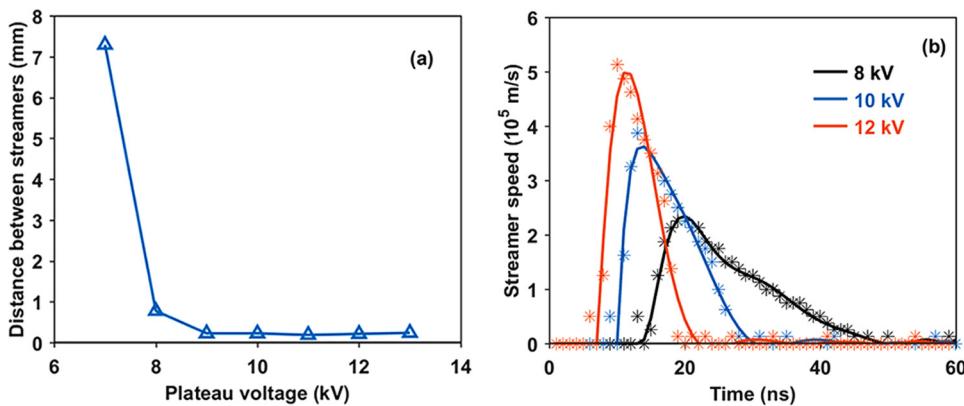


FIG. 9. (a) Ultimate separation distance between the heads of counter-propagating streamers as a function of the plateau value of the voltage pulse for the two electrode-array. Identical voltage pulses [Fig. 1(c)] were applied to the two electrodes. Other parameters were at their base case values. (b) Streamer propagation speed as a function of time at different plateau voltages.

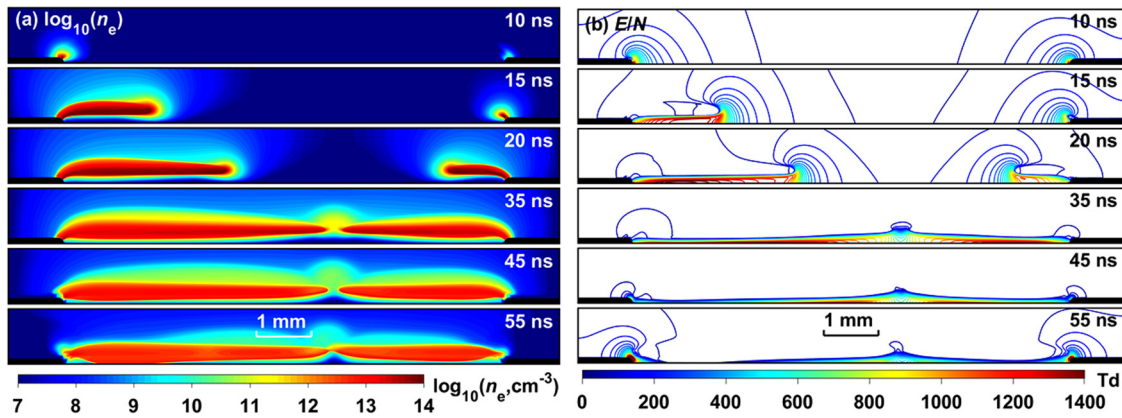


FIG. 10. Spatial distribution of $\log_{10}(n_e)$, n_e in cm^{-3} (a), and magnitude of reduced electric field E/N (b) for different times during a voltage pulse, in the two electrode-array configuration. In (b), the spacing between adjacent contours is 50 Td. The plateau voltage was 10 kV and 8 kV on the left and right electrodes, respectively. Other parameters were at their base case values. The 1 mm scale is shown at the bottom of the figure. Color scales of the E/N strength and the \log_{10} of the electron density are also shown.

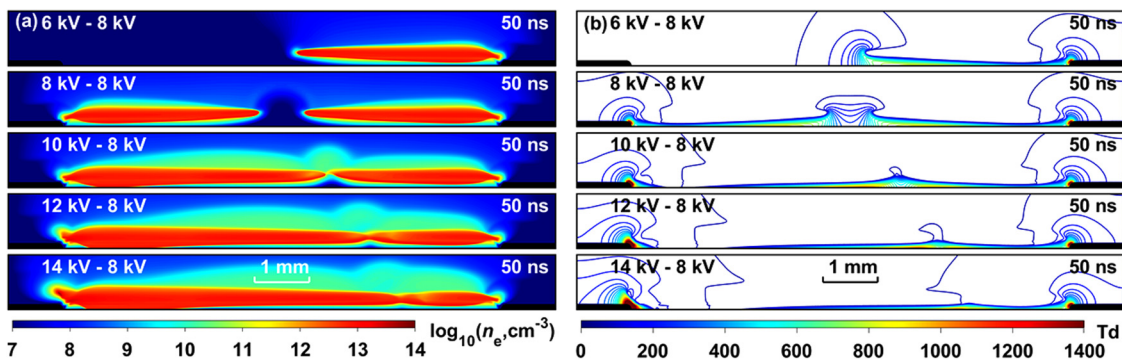


FIG. 11. Spatial distribution of $\log_{10}(n_e)$, n_e in cm^{-3} (a), and magnitude of reduced electric field E/N (b), at 50 ns with different plateau voltage pairs applied to the electrodes of a two-electrode array. In (b), the spacing between adjacent contours is 50 Td. In the voltage pairs shown, the left (right) voltage was applied to the left (right) electrode, respectively. Other parameters were at their base case values. The 1 mm scale is shown at the bottom of the figure. Color scales of the E/N strength and the \log_{10} of the electron density are also shown.

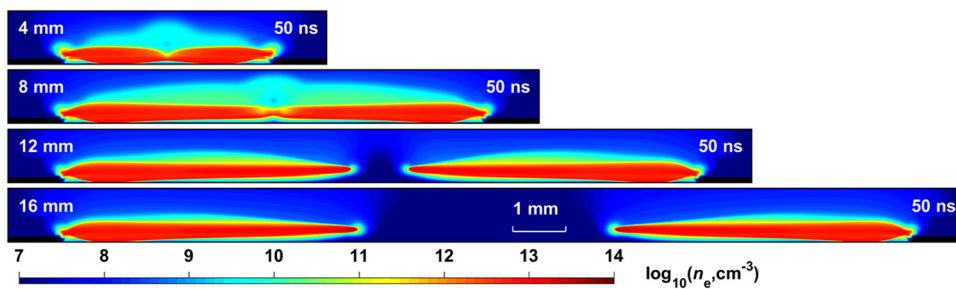


FIG. 12. Spatial distribution of $\log_{10}(n_e)$ at 50 ns in a two electrode-array [Fig. 7(a)], with variable spacing between the electrode edges. Electrode spacing from top to bottom is 4 mm, 8 mm, 12 mm, and 16 mm. Other parameters were at their base case values. The 1 mm scale is shown at the bottom of the figure. A color scale of the \log_{10} of the electron density is also shown.

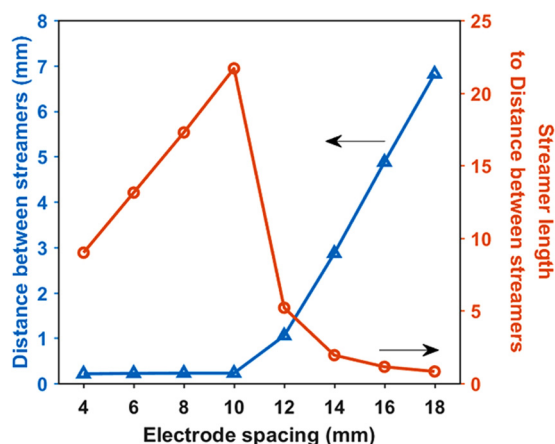


FIG. 13. Distance between counter-propagating streamers at the end of the voltage pulse (50 ns), and the ratio of streamer length to distance between streamers, as a function of spacing between the electrode edges in the two electrode-array.

voltage of 10 kV. The spacing between the facing edges of the two exposed electrodes was 8 mm. This spacing is shorter than twice the length (2×5.5 mm) of a streamer formed with a single exposed electrode (Fig. 2). One observes that, for the two electrode-array, each streamer length is shortened to ~ 3.9 mm, despite the fact that conditions are otherwise the same with the single exposed electrode micro-discharge. The minimum distance between the two streamer heads is ~ 0.2 mm. This is reached at 35 ns. Addition of a second exposed electrode not only shortens the streamer length but also weakens the discharge intensity, especially when the two counter-propagating streamers collide with each other. The discharge weakening can be explained by considering the head electric field. The high electric field in the streamer head is responsible for ionization

of neutrals to sustain the discharge and enable streamer propagation. When the two counter-propagating streamers approach each other, the opposite directed electric fields add up (to a large extent) destructively, reducing the net magnitude of E at the combined streamer heads, which results in weakening of the discharge. Figure 8(a) also shows the “second stroke” of the micro-discharge at 45 ns and 55 ns (see the discussion of Fig. 2).

Making the counter-propagating streamers merge, by shortening the (ultimate) distance between the streamer heads, can improve the uniformity of surface treatment. To that end, two approaches were tested: increase the plateau value of the applied voltage pulse and/or reduce the spacing between the exposed electrodes. Increasing the voltage reduces the ultimate distance between the streamers [Fig. 9(a)]. However, with further increases in voltage, the ultimate distance between the streamers appears to reach a (non-zero) minimum at high applied voltages, implying that the streamers cannot completely merge. In the streamer head, positive ions are ahead of negative ions and electrons, resulting in a strong electric field, necessary for the streamer to propagate. As the two counter-propagating streamers approach each other, the positive ion clouds encounter repulsive forces, caused by Coulomb interactions, preventing complete merging of the streamers.

The speed of the counter-propagating streamers in the two-electrode array is shown in Fig. 9(b). As the value of the plateau of the applied voltage pulse increases, the maximum speed of the streamers also increases and their deceleration after that maximum is sharper. In this case, for a plateau voltage of 10 kV, the streamer speed goes to zero at about 30 ns into the voltage pulse. This should be compared to the single electrode case [Fig. 4(b)], where the streamer speed goes to zero when the applied voltage is turned off at 50 ns. Similar results of streamer speed vs applied voltage were reported by Nishida and Abe.³²

Figure 10 shows results for the two electrode-array but with different voltage amplitudes, 10 kV on the left electrode and 8 kV on the right electrode. The discharge structure is no longer symmetric. Since the left streamer is more energetic (higher applied

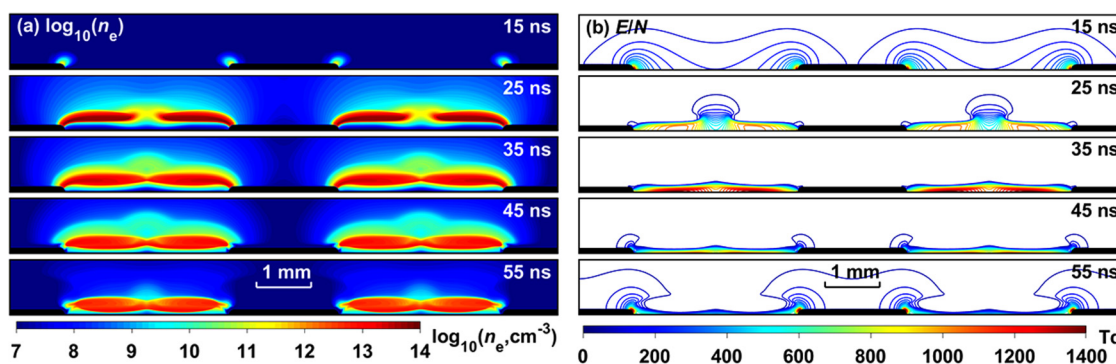


FIG. 14. Spatial distribution of $\log_{10}(n_e)$ with n_e in cm^{-3} (a), and magnitude of reduced electric field E/N (b) for different times during a voltage pulse, in the three electrode-array configuration [Fig. 7(b)]. Identical voltage pulses were applied to the three electrodes with a plateau of 8 kV. Other parameters were at their base case values. In (b), the spacing between adjacent contours is 50 Td. The 1 mm scale is shown at the bottom of the figure. Color scales of the E/N strength and the \log_{10} of the electron density are also shown.

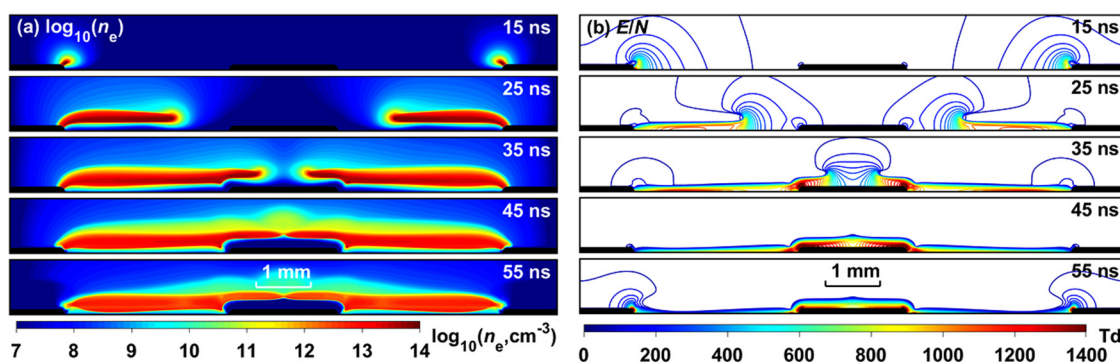


FIG. 15. Spatial distribution of $\log_{10}(n_e)$ (a), and magnitude of reduced electric field E/N (b) for different times during a voltage pulse, in the three electrode-array configuration [Fig. 7(b)]. Identical voltage pulses were applied to the left and right electrodes with a plateau of 8 kV, while the middle electrode was grounded. Other parameters were at their base case values. In Fig. 11(b), the spacing between adjacent contours is 50 Td. The 1 mm scale is shown at the bottom of the figure. Color scales of the E/N strength and the \log_{10} of the electron density are also shown.

voltage), propagating with higher speed, it occupies a larger fraction of the spacing between the electrodes. Streamer propagation seems to cease when the streamers collide with each other at 35 ns. Further increase of the left electrode voltage (keeping the right electrode voltage unchanged) results in more squeezing of the right streamer, as seen in Fig. 11.

This figure also shows that for a constant voltage V_{ar} applied to the right electrode, the (ultimate) distance between the streamers decreases as the voltage on the left electrode increases beyond V_{ar} . This fact, combined with the redistribution of the streamer lengths as the applied voltages vary, provides a convenient way to improve uniformity by optimizing the applied voltages.

A computational investigation of a SDBD with two exposed electrodes was reported by Kourtzanidis and Raja.²¹ The third electrode was powered by a negative voltage pulse. The negative voltage increases the gradient of potential in the discharge space compared with the present results of Fig. 8, employing a positive voltage pulse on the third electrode that actually reduces the gradient of potential. Although the two discharges are substantially different, in both cases the streamers cover the entire inter-electrode space.

In order to see the effect of electrode spacing on discharge uniformity, the two exposed electrode-array is considered again, and the results are shown in Figs. 12 and 13. The streamer length increases with electrode spacing but the (ultimate) distance between streamers also increases with spacing (Fig. 12). The ratio of streamer length to streamer (ultimate) distance vs electrode spacing is plotted in Fig. 13 as a proxy for uniformity. Clearly, there exists an optimum spacing maximizing uniformity.

A 2 mm-wide third (exposed) electrode was added between the left and right electrodes [see Fig. 7(b)] making the spacing between adjacent electrode edges only 3 mm. Identical voltage pulses [Fig. 1(c)] with a plateau value of 8 kV were applied to all three electrodes. Four streamers appeared at the exposed electrode edges (Fig. 14). At 35 ns, the counter-propagating streamers reach their minimum (ultimate) separation distance, then the intensity of the streamers gradually declines. The situation where the middle electrode is grounded, while the edge electrodes are powered with

voltage pulses (8 kV plateau), is shown in Fig. 15. This electrode-array configuration was studied experimentally in Ref. 53. Under these circumstances, streamers are ignited only at the edges of the left and right electrodes and propagate toward the middle electrode. When they reach the middle electrode, the streamers slide over that electrode and collide at the center of the electrode structure.

It should be noted that gas heating effects were not included in the simulation reported in this work. A constant temperature of 300 K was assumed. It was thought that heat transfer occurs on much longer time scales (e.g., ms) compared to a single voltage pulse considered (ns); therefore, heat affects would not be of any significance. However, in practical systems, employing multiple pulses, gas heating may be important, causing dilatational actuation of the flow, in addition to the basic electrostatic forcing. Furthermore, there is evidence of heat effects occurring over short time scales (tens of ns). This has been attributed to ultrafast energy deposition in the gas by dissociation of highly excited electronic states of O_2 , produced by electron-impact of ground state O_2 and/or by O_2 quenching of excited states of nitrogen [$N_2(B)$ and $N_2(C)$].²¹

IV. CONCLUSIONS

In this work, a 2D self-consistent fluid model was developed to study surface dielectric barrier discharges (SDBDs) with multiple exposed electrodes (electrode-array) powered by high voltage positive nanosecond pulses. Conclusions are summarized as follows:

1. During the ramp down of a voltage pulse, the contribution to the Laplacian electric field (zero net charge everywhere) due to the electrodes alone gradually declines, and the electric field due to the space charge and the accumulated surface charge becomes dominant. This results in electric field reversal referred to as the “second stroke.”
2. The volumetric force exerted by momentum transfer between charged species and the neutral gas is important for applications of SDBDs in aerodynamic flow control. This force mainly

appears in the cathode sheath and the streamer head. In the cathode sheath, the force pushes the neutral gas toward the dielectric surface, and the force extends all along the streamer length. At the streamer head, the force is much stronger and has a significant directed component that pushes the neutral gas downstream.

- Multiple exposed electrodes (electrode-array) may be used to increase the force on the neutral gas and/or to treat larger areas. In the latter case, discharge uniformity is an important consideration. When two counter-propagating streamers collide, the streamers come to a stop within a certain (ultimate) distance between the streamer heads. This is due to Coulombic repulsion of the positive ion clouds, in the leading edge of the streamer heads.
- Increasing the applied voltage reduces the ultimate distance between counter-propagating streamers, improving discharge uniformity. The ultimate distance between the streamers appears to saturate to a (non-zero) minimum at high applied voltages, implying that the streamers cannot merge completely.
- For a constant voltage V_{ar} applied to the right electrode of a two-electrode array, the (ultimate) distance between the streamers decreases as the voltage on the left electrode increases beyond V_{ar} . This fact, in combination with the redistribution of the streamer lengths as the voltages applied to the electrodes vary, provides a convenient way to improve uniformity by optimizing the applied voltages.
- In the electrode-array, the streamer length increases with increasing electrode spacing, but the ultimate distance between streamers also increases with spacing. The ratio of streamer length to streamer ultimate distance can be considered a proxy for discharge uniformity. It turns out that there exists an optimum electrode spacing maximizing the uniformity.

ACKNOWLEDGMENTS

Financial support of this work was provided by the National Natural Science Foundation of China (Nos. 11505020 and 11775043). D.J.E. acknowledges financial support by the US Department of Energy, Office of Fusion Energy Science (DE-SC0001939).

DATA AVAILABILITY

The data that support the findings of this study are available from the authors upon reasonable request.

REFERENCES

- D. B. Graves, *Phys. Plasmas* **21**, 080901 (2014).
- T. Von Woedtke, H. R. Metelmann, and K. D. Weltmann, *Contrib. Plasma Phys.* **54**, 104 (2014).
- M. Laroussi, X. Lu, and M. Keidar, *J. Appl. Phys.* **122**, 020901 (2017).
- G. Neretti, A. Cristofolini, and C. A. Borghi, *J. Appl. Phys.* **115**, 163304 (2014).
- E. Manirakiza, T. Seto, S. Osone, K. Fukumori, and Y. Otani, *Aerosol Sci. Technol.* **47**, 60 (2013).
- J. Zhang, Y. H. Wang, and D. Z. Wang, *IEEE Trans. Plasma Sci.* **46**, 19 (2018).
- S. Reuter, T. Von Woedtke, and K.-D. Weltmann, *J. Phys. D Appl. Phys.* **51**, 233001 (2018).

- A. A. Abdelaziz, T. Ishijima, T. Seto, N. Osawa, H. Wedaa, and Y. Otani, *Plasma Sources Sci. Technol.* **25**, 035012 (2016).
- V. Likhanskii, M. N. Shneider, S. O. Macheret, and R. B. Miles, *J. Appl. Phys.* **103**, 053305 (2008).
- P. Boeuf and L. C. Pitchford, *J. Appl. Phys.* **97**, 103307 (2005).
- V. Likhanskii, M. N. Shneider, S. O. Macheret, and R. B. Miles, *Phys. Plasmas* **14**, 073501 (2007).
- M. G. Kong, G. Kroesen, G. Morfill, T. Nosenko, T. Shimizu, J. Van Dijk, and J. L. Zimmermann, *New J. Phys.* **11**, 115012 (2009).
- V. R. Soloviev, V. M. Krivtsov, S. A. Shcherbanev, and S. M. Starikovskaia, *Plasma Sources Sci. Technol.* **26**, 014001 (2017).
- V. R. Soloviev and V. M. Krivtsov, *J. Phys. D Appl. Phys.* **42**, 125208 (2009).
- N. Y. Babaeva, D. V. Tereshonok, and G. V. Naidis, *Plasma Sources Sci. Technol.* **25**, 044008 (2016).
- R. Dawson and J. Little, *J. Appl. Phys.* **113**, 103302 (2013).
- R. A. Dawson and J. Little, *J. Appl. Phys.* **115**, 043306 (2014).
- T. Homola, R. Krumpolec, M. Zemanek, J. Kelar, P. Synek, T. Hoder, and M. Cernak, *Plasma Chem. Plasma Process.* **37**, 1149 (2017).
- G. Nayak, H. A. Aboubakr, S. M. Goyal, and P. J. Bruggeman, *Plasma Process. Polym.* **15**, 1700119 (2018).
- Z. Zhao, W. Wang, D. Yang, X. Zhou, and H. Yuan, *IEEE Trans. Plasma Sci.* **47**, 4219 (2019).
- K. Kourtzanidis and L. L. Raja, *AIAA J.* **55**, 1393 (2017).
- N. Y. Babaeva and M. J. Kushner, *Plasma Sources Sci. Technol.* **23**, 015007 (2014).
- M. Ghasemi, P. Olszewski, J. W. Bradley, and J. L. Walsh, *J. Phys. D Appl. Phys.* **46**, 052001 (2013).
- S. Wu and X. Lu, *Phys. Plasmas* **21**, 023501 (2014).
- W. Yan, F. Liu, C. Sang, and D. Wang, *Phys. Plasmas* **21**, 063505 (2014).
- J. Zhang, Y. Wang, and D. Wang, *Phys. Plasmas* **25**, 072101 (2018).
- I. V. Bozhko, I. P. Kondratenko, and Y. V. Serdyuk, *IEEE Trans. Plasma Sci.* **39**, 1228 (2011).
- H. Nishida, T. Nonomura, and T. Abe, *J. Appl. Phys.* **115**, 133301 (2014).
- A. Bourdon, V. P. Pasko, N. Y. Liu, S. Celestin, P. Segur, and E. Marode, *Plasma Sources Sci. Technol.* **16**, 656 (2007).
- D. Breden, K. Miki, and L. L. Raja, *Plasma Sources Sci. Technol.* **21**, 034011 (2012).
- J. P. Boeuf, Y. Lagmich, and L. C. Pitchford, *J. Appl. Phys.* **106**, 023115 (2009).
- H. Nishida and T. Abe, *J. Appl. Phys.* **110**, 013302 (2011).
- D. L. Scharfetter and H. K. Gummel, *IEEE Trans. Electron Devices* **16**, 64 (1969).
- G. E. Georgioui, A. P. Papadakis, R. Morrow, and A. C. Metaxas, *J. Phys. D: Appl. Phys.* **38**, R303 (2005).
- See <http://www.bolsig.laplace.univ-tlse.fr/> for information about Bolsig+.
- See www.lxcat.net for Morgan database; accessed 1 March 2018.
- See www.lxcat.net for TRINITI database; accessed 2 March 2018.
- See www.lxcat.net for Phelps database; accessed 2 March 2018.
- J. Perrin, O. Leroy, and M. C. Bordage, *Contrib. Plasma Phys.* **36**, 3 (1996).
- S. Celestin, Z. Bonaventura, B. Zeghondy, A. Bourdon, and P. Segur, *J. Phys. D Appl. Phys.* **42**, 065203 (2009).
- See <http://crd-legacy.lbl.gov/~xiaoye/SuperLU/> for information about SuperLU.
- M. Moravej, X. Yang, M. Barankin, J. Penelon, S. E. Babayan, and R. F. Hicks, *Plasma Sources Sci. Technol.* **15**, 204 (2006).
- I. A. Kossyi, A. Y. Kostinsky, A. A. Matveyev, and V. P. Silakov, *Plasma Sources Sci. Technol.* **1**, 207 (1992).
- O. Eichwald, M. Yousfi, A. Hennad, and M. D. Benabdessadok, *J. Appl. Phys.* **82**, 4781 (1997).
- S. Pancheshnyi, M. Nudnova, and A. Starikovskii, *Phys. Rev. E* **71**, 016407 (2005).
- T. Murakami, K. Niemi, T. Gans, D. O'connell, and W. G. Graham, *Plasma Sources Sci. Technol.* **22**, 015003 (2013).
- D. S. Stafford and M. J. Kushner, *J. Appl. Phys.* **96**, 2451 (2004).

- ⁴⁸X. Y. Liu, X. K. Pei, X. P. Lu, and D. W. Liu, *Plasma Sources Sci. Technol.* **23**, 035007 (2014).
- ⁴⁹R. Atkinson, D. L. Baulch, R. A. Cox, R. F. Hampson, J. A. Kerr, M. J. Rossi, and J. Troe, *J. Phys. Chem. Ref. Data* **26**, 521 (1997).
- ⁵⁰R. A. Arakoni, N. Y. Babaeva, and M. J. Kushner, *J. Phys. D Appl. Phys.* **40**, 4793 (2007).
- ⁵¹Y. Sakiyama, D. B. Graves, H. W. Chang, T. Shimizu, and G. E. Morfill, *J. Phys. D Appl. Phys.* **45**, 425201 (2012).
- ⁵²B. Peng, N. Jiang, X. Yao, Y. Ruan, D. Wang, K. Shang, N. Lu, T. Namihira, J. Li, and Y. Wu, *J. Phys. D Appl. Phys.* **52**, 325202 (2019).
- ⁵³K. D. Bayoda, N. Benard, and E. Moreau, *J. Appl. Phys.* **118**, 063301 (2015).
- ⁵⁴D. X. Liu, Z. C. Liu, C. Chen, A. J. Yang, D. Li, M. Z. Rong, H. L. Chen, and M. G. Kong, *Sci. Rep.* **6**, 23737 (2016).
- ⁵⁵S. Sato, H. Furukawa, A. Komuro, M. Takahashi, and N. Ohnishi, *Sci. Rep.* **9**, 5813 (2019).